PHYSICAL REVIEW B **109**, 184426 (2024)

Non-Hermitian spin dynamics in a coupled ferrimagnetic system

Xue Zhang,[1,*] Changjiang Liu,[2,*] Zhifeng Zhu,[1,†] and Yue Zhang[2,‡]
[1]*School of Information Science and Technology, ShanghaiTech University, Shanghai 201210, China*
[2]*School of Integrated Circuit, Huazhong University of Science and Technology, Wuhan 430074, 2201, China*

(Received 19 November 2023; revised 1 April 2024; accepted 30 April 2024; published 13 May 2024)

The interplay of non-Hermitian (NH) spin dynamics in coupled ferromagnetic (FM) systems has unveiled intriguing phenomena, notably the manifestation of FM-antiferromagnetic (AFM) phase transitions at exceptional points (EPs). Extending beyond traditional FM media, ferrimagnetic (FiM) media combine the advantages of AFM and FM systems, displaying distinct attributes especially at the angular momentum composition (AMC) point, x_{AMC}. This study explores the profound influence of FiM composition on the NH spin dynamics of a coupled FiM system. At x_{AMC}, the spin dynamics depicted by the Néel vector demonstrates a parity-time ($\mathcal{PT}$) symmetry, exhibiting power-law frequency splitting concerning external perturbations at the EP with a fixed power of 1/2. However, deviation from x_{AMC} leads to partial converging of eigenfrequency branches at the EP owing to the uncompensated angular momentum, displaying power-law frequency splitting with varied powers, akin to an effective coupled RLC circuit with capacitance influenced by frequency variations. This investigation opens a unique avenue in the area of $\mathcal{PT}$ symmetry in magnetic NH systems, unraveling the nuanced behaviors of coupled FiM configurations.

DOI: 10.1103/PhysRevB.109.184426

I. INTRODUCTION

A ferrimagnetic (FiM) medium is composed of two sublattices of magnetic moments (spins) oriented in opposite direction with different magnitudes. The properties of FiM systems are intricately tied to the ratio of the spins (magnetic moments) between these two sublattices. Because of differing gyromagnetic ratios of the elements the FiM medium comprises, there exists a special angular momentum composition (AMC) point, x_{AMC}, where the net spin diminishes while the net magnetic moment remains nonzero.

At x_{AMC}, a FiM medium exhibits ultrafast antiferromagnetic (AFM) spin dynamics with detectable signals owing to the uncompensated magnetic moments [1]. Furthermore, the FiM medium at x_{AMC} displays several remarkable characteristics. For example, the frequency of spin oscillation and the Gilbert damping parameter experience a significant increase in proximity to x_{AMC} [2]. Additionally, the velocity of domain walls or skyrmions achieves its maximum value near x_{AMC} [3,4]. Recent predictions also suggest an augmentation of magnon-magnon entanglement within a cavity of FiM magnons coupled with photons at x_{AMC} [5].

In addition to these magnetic properties, the study of non-Hermitian (NH) [6–8] spin dynamics within a coupled magnetic medium has attracted wide attention in recent years. Here, NH dynamics features complex eigenvalues resulting from the breaking of parity-time ($\mathcal{PT}$) symmetry [9–12]. This is in contrast to conventional Hermitian systems in quantum mechanics. In an NH system, the breaking of $\mathcal{PT}$ symmetry ($\mathcal{PT}$ transition) at exceptional points (EPs) [13–17] is identified by the convergence of the real parts of the eigenfrequencies, accompanied by the emergence of nonzero imaginary components [18]. Additionally, the eigenfrequencies undergo sensitive splitting at the EP when subjected to external perturbations. The frequency splitting (Δf) satisfies a power-law relationship with the perturbation (ε), with the power determined by the EP order [19–23].

Until now, research of NH spin dynamics has predominantly focused on the coupled ferromagnetic (FM) system [22,24–26]. In these studies, NH spin dynamics was primarily affected by the strength of coupling between the two FM media. It is anticipated that in an NH coupled FiM system, apart from the coupling strength, the spin ratio between the two sublattices, particularly in proximity to x_{AMC}, could also profoundly influence NH spin dynamics. Nevertheless, exploration regarding the influence of FiM composition on NH spin dynamics remains an open area.

In this article, we theoretically investigate NH spin dynamics in a coupled FiM system, especially emphasizing the effect of FiM composition on NH spin dynamics. At x_{AMC}, the FiM medium exhibits $\mathcal{PT}$ symmetry, displaying power-law frequency splitting at the EP concerning external perturbations with a fixed power of 1/2. However, deviation from x_{AMC} results in convergence of partial eigenfrequency branches at EPs, demonstrating power-law frequency splitting with varying powers due to the existence of a nonzero net spin, which resembles a frequency-dependent capacitance in a coupled RLC circuit.

II. MODEL AND THEORY

We investigated the multilayer system FiM layer I/heavy metal (HM)/FiM layer II, incorporating Ruderman-Kittel-Kasuya-Yosida (RKKY) coupling between the two FiM

---

[*] These authors contributed equally to this work.
[†] Corresponding author: zhuzhf@shanghaitech.edu.cn
[‡] Corresponding author: yue-zhang@hust.edu.cn

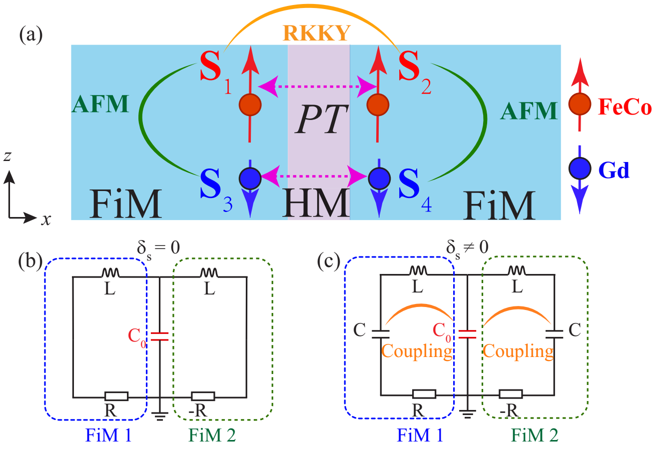

FIG. 1. (a) Schematic of a coupled FiM system, including two FiM layers with a heavy metal layer. In equilibrium, the spin angular momentum aligns predominantly along the z direction. In this coupled FiM system, the spin angular momenta governed by RKKY coupling adhere to $\mathcal{PT}$ symmetry. The equivalent circuit of two coupled RLC circuits corresponding to (b) $\delta_s = 0$ and (c) $\delta_s \neq 0$. The two RLC circuits mirror the two FiM systems, where the capacitance C_0 symbolizes the RKKY coupling. The frequency-dependent capacitance serves as an analogy to the FiM system experiencing a composition deviation from the angular compensation point.

$[(\mathrm{FeCo})_{1-x_G}(\mathrm{Gd})_{x_G}]$ alloy layers [Fig. 1(a)]. Specifically, our study focused on the FM RKKY coupling between the two FiM layers, characterized by the exchange energy J_R. Within each FiM layer, the antiparallel spin alignment in the FeCo and Gd sublattices was stabilized by intralayer AFM exchange energy, denoted as J_A. We fixed J_A as 1.09×10^{-21} J [2] and J_R varies between zero and 3.815×10^{-23} J, which is on the order of RKKY strength [27]. For simplicity, we neglected the potential coupling between $\mathbf{S}_1$ and $\mathbf{S}_4$, as well as between $\mathbf{S}_2$ and $\mathbf{S}_3$. This coupling may become zero at a specific thickness of the HM layer due to the abrupt sign-switching behavior of the RKKY coupling with the distance between two spins [28].

The average saturation magnetizations of FeCo (Gd) in the two FiM layers were labeled as $M_1(M_3) = M_2(M_4) = M_\alpha(M_\beta)$. We defined $M_\alpha = (1 - x_G)M_\mathrm{FeCo}$ and $M_\beta = x_G M_\mathrm{Gd}$, where M_FeCo and M_Gd represent the saturation magnetizations for FeCo and Gd, respectively. The magnitudes of the spin angular momenta for FeCo and Gd are $S_\alpha = M_\alpha/\gamma_\alpha$ and $S_\beta = M_\beta/\gamma_\beta$, respectively, where γ_α and γ_β are the gyromagnetic ratios of FeCo and Gd, respectively. We defined $\delta_\mathrm{s} = (M_\alpha/\gamma_\alpha) - (M_\beta/\gamma_\beta)$ to illustrate the deviation of composition from the angular momentum compensation point. Based on the parameters [2,29,30] $M_\mathrm{FeCo} = 3.21 \times 10^5$ A/m, $M_\mathrm{Gd} = 1.10 \times 10^6$ A/m, $\gamma_\mathrm{FeCo} = 1.93 \times 10^{11}$ 1/(s T), $\gamma_\mathrm{Gd} = 1.76 \times 10^{11}$ 1/(s T), and the atomic magnetic moments of Fe and Gd, $\mu_\mathrm{Fe} = 1.92\mu_\mathrm{B}$ and $\mu_\mathrm{Gd} = 7.63\mu_\mathrm{B}$, $\delta_\mathrm{s} = 0$ corresponds to $x_\mathrm{AMC} = 0.21$.

We started via the Landau-Lifshitz-Gilbert (LLG) equations based on a macrospin model:

$$\dot{\vec{S}}_1 = -\gamma_\alpha \vec{S}_1 \times (J_R \vec{S}_2 + J_A \vec{S}_3) + \alpha \vec{S}_1 \times \dot{\vec{S}}_1, \tag{1}$$

$$\dot{\vec{S}}_3 = -\gamma_\beta \vec{S}_3 \times (J_A \vec{S}_1 + J_R \vec{S}_4) + \alpha \vec{S}_3 \times \dot{\vec{S}}_3, \tag{2}$$

$$\dot{\vec{S}}_2 = -\gamma_\alpha \vec{S}_2 \times (J_R \vec{S}_1 + J_A \vec{S}_4) - \alpha \vec{S}_2 \times \dot{\vec{S}}_2, \tag{3}$$

$$\dot{\vec{S}}_4 = -\gamma_\beta \vec{S}_4 \times (J_A \vec{S}_2 + J_R \vec{S}_3) - \alpha \vec{S}_4 \times \dot{\vec{S}}_4\,. \tag{4}$$

In a real coupled FiM system, the spin dynamics equations can become more intricate. Several complex factors, such as the coupling between $\mathbf{S}_1$ and $\mathbf{S}_4$ and between $\mathbf{S}_2$ and $\mathbf{S}_3$, differences in damping coefficients between $\mathbf{S}_1$ ($\mathbf{S}_2$) and $\mathbf{S}_3$ ($\mathbf{S}_4$), and cross-damping terms between different spins, may need consideration. The influence of these additional factors on the NH dynamics of the coupled FiM system is addressed in the Supplemental Material [31] (see also Refs. [16,32] therein).

In the linear approximation, the spin was described as $\vec{S}_i = S_{is}\vec{e}_z + (s_{ix}\vec{e}_x + s_{iy}\vec{e}_y)e^{-i\omega t}$. Here $S_{is} = |S_i|$ for $i = 1, 2$, and $S_{is} = -|S_i|$ for $i = 3, 4$. To maintain $\mathcal{PT}$ symmetry, the effective damping coefficients in the two FiM layers are denoted as α and $-\alpha$, respectively. In this work, we considered a fixed value of $\alpha = 0.02$. By introducing the wave function $\psi_i = s_{ix} - is_{iy}$, the LLG equations were converted to $\omega\begin{bmatrix}\psi_1\\ \psi_2\\ \psi_3\\ \psi_4\end{bmatrix} = \mathbf{H}\begin{bmatrix}\psi_1\\ \psi_2\\ \psi_3\\ \psi_4\end{bmatrix}$, where the Hamiltonian $\mathbf{H}$ is shown as below (please refer to Appendix A for more detailed information about the derivation):

$$\mathbf{H} = \begin{bmatrix} \frac{-D_\mathrm{I}}{(1+i\alpha)} & \frac{A_\mathrm{I}}{(1+i\alpha)} & \frac{B_\mathrm{I}}{(1+i\alpha)} & 0 \\ \frac{A_\mathrm{I}}{(1-i\alpha)} & \frac{-D_\mathrm{I}}{(1-i\alpha)} & 0 & \frac{B_\mathrm{I}}{(1-i\alpha)} \\ \frac{A_\mathrm{II}}{(1+i\alpha)} & 0 & \frac{-D_\mathrm{II}}{(1+i\alpha)} & \frac{B_\mathrm{II}}{(1+i\alpha)} \\ 0 & \frac{A_\mathrm{II}}{(1-i\alpha)} & \frac{B_\mathrm{II}}{(1-i\alpha)} & \frac{-D_\mathrm{II}}{(1-i\alpha)} \end{bmatrix}. \tag{5}$$

For the interchange of the spin pair in the coupled FiM system [between S_1 (S_3) and S_2 (S_4)], the matrix representation of P is given by $P = \begin{pmatrix} 0 & 1 & 0 & 0\\ 1 & 0 & 0 & 0\\ 0 & 0 & 0 & 1\\ 0 & 0 & 1 & 0\end{pmatrix}$. From this P operation, it becomes evident that $\mathbf{H}$ satisfies $\mathcal{PT}$ symmetry as $(\mathbf{PT})\mathbf{H}(\mathbf{PT})^{-1} = \mathbf{H}$. Here $\mathbf{T}$ means the time-reversal operation, which satisfies $\mathbf{THT}^{-1} = \mathbf{H}^*$, with $\mathbf{H}^*$ denoting the complex conjugation of $\mathbf{H}$. In addition to that, the block matrix elements $H_{11} = \begin{bmatrix} \frac{-D_\mathrm{I}}{(1+i\alpha)} & \frac{A_\mathrm{I}}{(1+i\alpha)} \\ \frac{A_\mathrm{I}}{(1-i\alpha)} & \frac{-D_\mathrm{I}}{(1-i\alpha)} \end{bmatrix}$ and $H_{22} = \begin{bmatrix} \frac{-D_\mathrm{II}}{(1+i\alpha)} & \frac{B_\mathrm{II}}{(1+i\alpha)} \\ \frac{B_\mathrm{II}}{(1-i\alpha)} & \frac{-D_\mathrm{II}}{(1-i\alpha)} \end{bmatrix}$ are also invariant under the $\mathcal{PT}$ operation. This scenario elucidates the presence of $\mathcal{PT}$ symmetry between the two pairs of spins governed by RKKY coupling, i.e., $(\mathbf{S}_1, \mathbf{S}_2)$ and $(\mathbf{S}_3, \mathbf{S}_4)$.

To clarify the influence of FiM composition on NH spin dynamics, we further deduced the spin dynamics equations of the coupled FiM system expressed by the Néel vector. We first defined the uniform magnetization $\mathbf{s}$ and Néel vector $\mathbf{n}$ as $\mathbf{s} = (\mathbf{s}_\alpha + \mathbf{s}_\beta)/2$ and $\boldsymbol{n} = (\mathbf{s}_\alpha - \mathbf{s}_\beta)/2$. Here $\mathbf{s}_\alpha$ and $\mathbf{s}_\beta$ are the unit magnetizations for FeCo and Gd, respectively. Under the linear approximation, the components of $\boldsymbol{n}_{\mathrm{I(II)}}$ can be written as $\mathbf{n}_{\mathrm{I(II)}} = \delta(n_{\mathrm{I(II)}}x, \delta n_{\mathrm{I(II)}}y, 1)$. Introducing $\Psi_{\mathrm{I(II)}} = \delta n_{\mathrm{I(II)}}x + \mathrm{i}\delta n_{\mathrm{I(II)}}y$, we derived the coupled dynamics

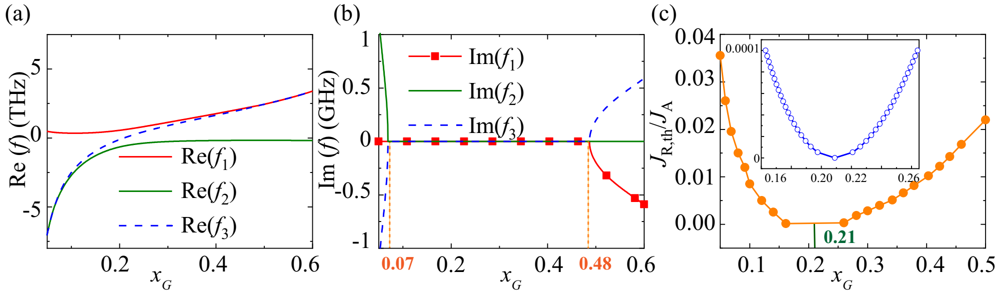

FIG. 2. (a) Real and (b) imaginary part of the eigenfrequency f as a function of x_G. (c) The threshold of J_R ($J_\mathrm{R,th}$) for the $\mathcal{PT}$ transition as a function of x_G. The $J_\mathrm{R,th}/J_\mathrm{A}$ approaches zero at x_AMC. The inset exhibits the subtle changes of $J_\mathrm{R,th}/J_\mathrm{A}$ near x_G.

equations for $\Psi_{\mathrm{I(II)}}$ as (please refer to Appendix B for more detailed information about the derivation)

$$\frac{\rho^2}{A_\mathrm{ex}}\ddot{\Psi}_\mathrm{I} - (\mathrm{i}\delta_s + \alpha\rho)\dot{\Psi}_\mathrm{I} + A_R\Psi_\mathrm{I} - A_R\Psi_\mathrm{II} = 0, \tag{6}$$

$$\frac{\rho^2}{A_\mathrm{ex}}\ddot{\Psi}_\mathrm{II} + (\mathrm{i}\delta_s - \alpha\rho)\dot{\Psi}_\mathrm{II} + A_R\Psi_\mathrm{II} - A_R\Psi_\mathrm{I} = 0. \tag{7}$$

Here $A_R = -J_R(M_\alpha^2 + M_\beta^2)$ and $A_\mathrm{ex} = 4J_AM_\alpha M_\beta$, and $\rho = (M_\alpha/\gamma_\alpha) + (M_\beta/\gamma_\beta)$.

Equations (6) and (7) delineate dynamics reminiscent of coupled inertial systems. It is noteworthy that an additional term, $-\mathrm{i}\delta_s\dot{\Psi}_{\mathrm{I(II)}}$, is incorporated when the composition deviates from x_AMC. To illustrate the function of $-\mathrm{i}\delta_s\dot{\Psi}_{\mathrm{I(II)}}$, we expressed $\Psi_{\mathrm{I(II)}} = \Psi_{\mathrm{I(II)}_0}\exp(-\mathrm{i}\omega t)$ and substituted it into Eqs. (6) and (7). Consequently, the resulting eigenvalue equations for $\Psi_{\mathrm{I(II)}_0}$ can be expressed as $\mathrm{H}_2\binom{\Psi_\mathrm{I0}}{\Psi_\mathrm{II0}} = 0$, with the Hamiltonian H_2 expressed as

$$\begin{pmatrix} \frac{\omega^2\rho^2}{A_\mathrm{ex}} - (A_R - \omega\delta_s) - \mathrm{i}\omega\alpha\rho & A_R \\ A_R & \frac{\omega^2\rho^2}{A_\mathrm{ex}} - (A_R - \omega\delta_s) + \mathrm{i}\omega\alpha\rho \end{pmatrix}. \tag{8}$$

Here a critical characteristic defining the coupled FiM system with uncompensated spin angular momentum is the $\omega\delta_\mathrm{S}$ term. This term, akin to a *frequency-relevant* factor, augments the parameter A_R, analogous to a stiffness constant in an elastic system. Notably, when $\delta_\mathrm{s} \neq 0$, the alteration in frequency under perturbation effectively modifies the stiffness constant of this elasticlike system. Consequently, this leads to a feedbacklike behavior, where changes in frequency modify the system's stiffness constant, leading to further changing of frequency.

It is intriguing to observe that Eqs. (6) and (7) bear a resemblance to the dynamics observed in a coupled RLC circuit [Figs. 1(b) and 1(c)] [33,34]. In this analogy, the wave function $\Psi_{\mathrm{I(II)}}$ aligns with the charge of the two capacitances, while parameters such as inductance (L), resistance (R), and capacitance (C) correspond to the inertia term, damping term, and the zero-order differential term concerning time in the spin dynamics equations for the coupled FiM system. Notably, the negative R can be achieved through feedback from a voltage-doubling buffer [35]. The coupling of the two capacitances by C_0 mirrors the RKKY coupling within the FiM system. In addition, the NH topolectrical circuit represents a viable option for expressing this coupled FiM system [36]. The inclusion of NH circuit components, such as NH dampers and nonlinear elements, streamlines the incorporation of gain and loss within the circuit.

In the context of the equivalent circuit, $\delta_\mathrm{s} = 0$ corresponds to an effectively infinite capacitance C, akin to a short-circuit effect observed in alternating current circuits [Fig. 1(b)]. Under these conditions, external perturbations, such as those induced by an electromagnetic field, do not influence the intrinsic capacitance of the RLC circuit. Conversely, when $\delta_\mathrm{s} \neq 0$, the capacitance becomes frequency dependent [Fig. 1(c)]. Consequently, alterations in frequency induced by external perturbations can further modify the capacitance, instigating a feedback effect that contributes to frequency variation. This feedback mechanism leads to changes in frequency due to the modifications in capacitance driven by external perturbations. This feedback frequency modulation will be verified by the varied power of the power-law frequency splitting at the EP that will be discussed below.

III. RESULTS AND DISCUSSION

A. Eigenfrequency and spin dynamics modes of the NH coupled FiM system

We draw the real and imaginary eigenfrequencies in Figs. 2(a) and 2(b) (please refer to Appendix C for more detailed information about the derivation).

Even though the coupled FiM system features three branches of frequencies (f_1, f_2, and f_3), it cannot be taken as a conventional third-order NH system with PT symmetry since not all three branches converge at a single fixed EP [19]. The real parts of f_2 and f_3 (f_1 and f_3) merge at two distinct EPs at $x_G = 0.07$ (0.48) [Fig. 2(a)]. This merging is accompanied by the emergence of imaginary parts of f_2 and f_3 (f_1 and f_3) at $x_G < 0.07$ ($x_G > 0.48$) [Fig. 2(b)]. This partial coalescence of the real eigenfrequencies stands as evidence indicating the partial PT symmetry within the coupled FiM system. Furthermore, the PT transition in this study diverges from the pairwise coalescence of a sequence of discrete eigenvalues observed in Bender's quantum-mechanics-based calculations [9]. In this work, within the three frequency branches, two distinct branches converge at separate EPs.

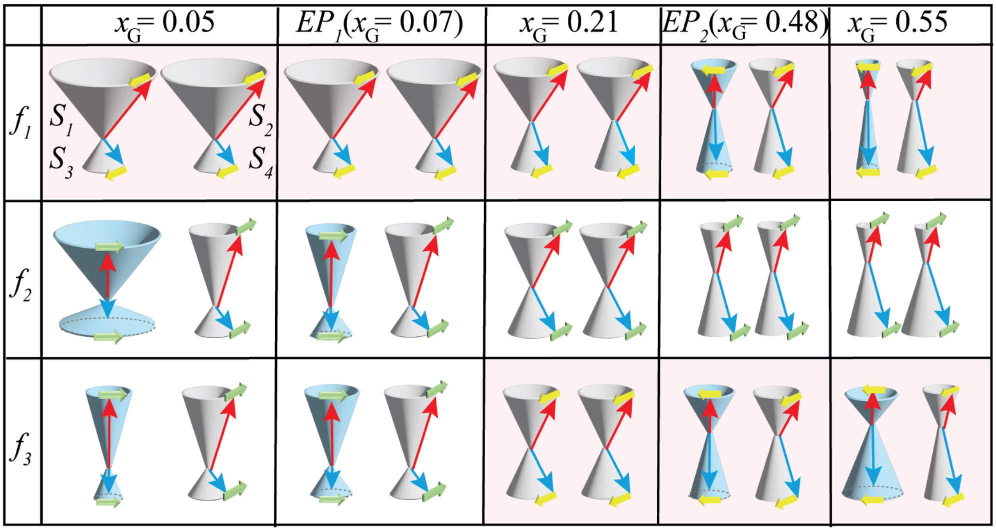

FIG. 3. The phase diagram for the spin precession at different eigenfrequencies in the coupled FiM system with different x_G.

The x_G values for the EPs can be adjusted by modifying the RKKY coupling [Fig. 2(c)]. Specifically, the two EPs merge at x_{AMC} ($\delta_s = 0$) when the critical J_R for the PT transition ($J_{R,\mathrm{th}}$) approached zero. Consequently, at $\delta_s = 0$, the PT transition occurs only when the J_R becomes zero. This state can be achieved at various thicknesses of the HM layer [27,37,38].

In addition to eigenfrequencies, the evolution of spin dynamics modes within the coupled FiM system serves as another indicator of partial PT symmetry. The phase diagram for the spin precession at different eigenfrequencies is presented in Fig. 3. Here the red and blue arrows denote the spins of FeCo and Gd, respectively. The yellow and green ones represent the directions for spin rotation. At f_1 (f_2), when $x_G < 0.48$ ($x_G > 0.07$), S_1 and S_3 satisfy the PT symmetry between S_2 and S_4, while the PT symmetry cannot be satisfied between S_1 and S_3 (S_2 and S_4). This illustrates partial PT symmetry. On the other hand, the PT transition occurs when x_G approaches the EPs, which was reflected from a 90 ° phase difference for the spin oscillation between the two FiM layers. This suggests the appearance of the imaginary part of the eigenfrequencies. When x_G approaches x_{AMC} for $\delta_s = 0$, the spin precession at f_3 changes its direction from counterclockwise to clockwise, which corresponds to the change of sign of f_3 in Fig. 2(b). Contrasting the phase diagram for the FM-AFM transition in the coupled FM-NH system [12,24], the focus of this work lies in the PT transition resulting from the modulation of the x_G, rather than the AFM-FM phase transition.

B. Splitting of eigenfrequencies (Δf) as a function of perturbation ε at the EPs

In addition to the convergence of eigenfrequencies, another vital characteristic of an NH system lies in Δf at the EP under the perturbation ε (Fig. 4). Typically, Δf follows a power-law relationship with ε, the exponent of which is determined by the order of the NH system [19]. In our analysis, we considered the perturbed Hamiltonian $\mathbf{H}_\varepsilon$ by adding ε to the first

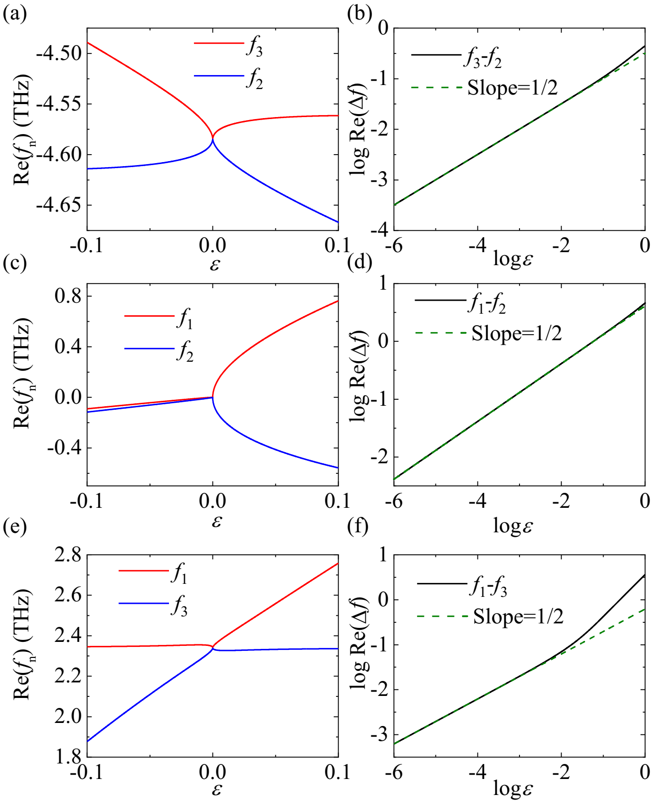

FIG. 4. The real part of eigenfrequency f as a function of perturbation ε for (a) $x_G = 0.07$, (c) x_{AMC}, and (e) $x_G = 0.48$. The frequency shift (b) $f_3 - f_2$, (d) $f_1 - f_2$, and (f) $f_1 - f_3$ as a function of ε in the logarithmic coordinates with the green dashed lines for the linear fitting using the 1/2 slope.

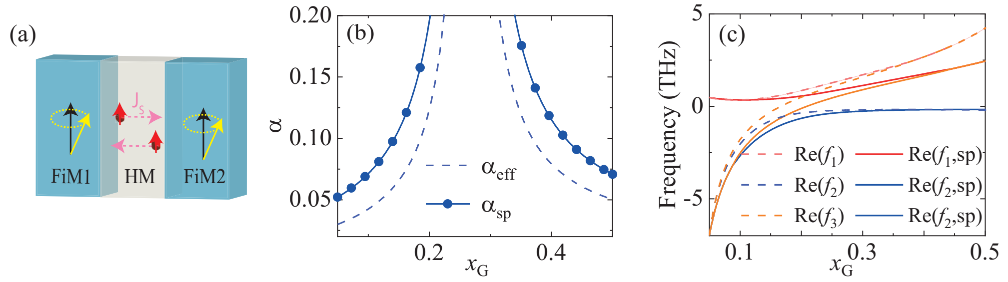

FIG. 5. Illustration of spin current propagation in the NM layer due to the spin pumping triggered by the spin precession in the FiM layers. (b) Original damping coefficients and the corrected values obtained by considering spin pumping as a function of x_G. (c) Original real part of the eigenfrequencies and the corrected values obtained by spin pumping as a function of x_G.

macrospin:

$$H_\varepsilon = \begin{bmatrix} \frac{-D_{\mathrm{I}}+\omega_0\varepsilon}{1+\alpha \mathrm{i}} & \frac{A_{\mathrm{I}}}{1+\alpha \mathrm{i}} & \frac{B_{\mathrm{I}}}{1+\alpha \mathrm{i}} & 0 \\ \frac{A_{\mathrm{I}}}{1-\alpha \mathrm{i}} & \frac{D_{\mathrm{I}}}{1-\alpha \mathrm{i}} & 0 & \frac{B_{\mathrm{I}}}{1-\alpha \mathrm{i}} \\ \frac{A_{\mathrm{II}}}{1+\alpha \mathrm{i}} & 0 & \frac{-D_{\mathrm{II}}}{1+\alpha \mathrm{i}} & \frac{B_{\mathrm{II}}}{1+\alpha \mathrm{i}} \\ 0 & \frac{A_{\mathrm{II}}}{1-\alpha \mathrm{i}} & \frac{B_{\mathrm{II}}}{1-\alpha \mathrm{i}} & \frac{-D_{\mathrm{II}}}{1-\alpha \mathrm{i}} \end{bmatrix},$$

where $\omega_0 = \gamma_\alpha J_A M_\beta$.

By derivation the eigenfrequencies of $\mathbf{H}_\varepsilon$ can be expressed as $f^4 + (k_3 + \varepsilon k_3')f^3 + (k_2 + \varepsilon k_2')f^2 + (k_1 + \varepsilon k_1')f + k_0 = 0$. Here k_i and k_i' represent the coefficients from the original determinant and the modified ones resulting from the introduction of ε, respectively. This equation, a fourth-order nonlinear equation, can be perturbatively expanded using the Newton-Puiseux series: $f_{\mathrm{n}} = c_{n0} + c_{n1}\varepsilon^{1/4} + c_{n2}\varepsilon^{1/2} + c_{n3}\varepsilon^{3/4} + c_{n4}\varepsilon$ with complex coefficients c_{ni} $(n = 1, 2, 3)$ [39]. Consequently, we obtain the analytical results of Δf as a function of ε for each pair of branches:

$$\mathrm{Re}(f_3 - f_2) = 0.31\varepsilon^{\frac{1}{2}} - 0.07\varepsilon^{\frac{3}{4}} + 0.22\varepsilon,$$

$$\mathrm{Re}(f_1 - f_2) = -0.04\varepsilon^{\frac{1}{4}} + 4.60\varepsilon^{\frac{1}{2}} - 1.51\varepsilon^{\frac{3}{4}} + 1.56\varepsilon,$$

$$\mathrm{Re}(f_1 - f_3) = 0.11\varepsilon^{\frac{1}{4}} - 0.38\varepsilon^{\frac{1}{2}} - 1.23\varepsilon^{\frac{3}{4}} + 2.68\varepsilon.$$

At x_{AMC} $(\delta_{\mathrm{s}} = 0)$, it is obvious that the $\varepsilon^{1/2}$ term is dominant over other terms, specifically observed in Re$(f_1 - f_2)$. This observation aligns well with the linear correlation between log(Δf) and log ε displaying a slope of 1/2 across a broad log ε range spanning from -6 to 0 [Fig. 4(d)]. Conversely, when $\delta_{\mathrm{s}} \neq 0$, besides the prominent $\varepsilon^{1/2}$ term, the influence of other higher-order terms becomes noticeable, notably the $\varepsilon^{3/4}$ and ε terms in Re$(f_2 - f_3)$ at $x_G = 0.48$. This observation corresponds to the gradual variation in the slope of log Δf versus log ε, as depicted in Figs. 4(b) and 4(f). The constant power for $\delta_{\mathrm{s}} = 0$ and the variation of power with ε for $\delta_{\mathrm{s}} \neq 0$ is consistent with the prediction based on the effective RLC circuit model as depicted in Fig. 1.

C. Influence of spin pumping on the NH spin dynamics in the coupled FiM systems

Finally, we consider the influence of spin pumping on the damping coefficient and the NH spin dynamics in the coupled FiM system [Fig. 5(a)].We first utilized the effective Gilbert damping (α_{eff}) of the FiM layer [2] as $\alpha_{\mathrm{eff}} = (\frac{\alpha_{\mathrm{FeCo}} M_{\mathrm{FeCo}}}{\gamma_{\mathrm{FeCo}}} + \frac{\alpha_{\mathrm{Gd}} M_{\mathrm{Gd}}}{\gamma_{\mathrm{Gd}}})/(\frac{M_{\mathrm{FeCo}}}{\gamma_{\mathrm{FeCo}}} - \frac{M_{\mathrm{Gd}}}{\gamma_{\mathrm{Gd}}})$ with the gyromagnetic ratio $\gamma_{\mathrm{Gd\ (FeCo)}}$, and the damping constant $\alpha_{\mathrm{Gd\ (FeCo)}}$.

Based on the theory of spin pumping, a spin current can be triggered and it flows into the nonmagnetic metal (NM) layer due to the spin precession in the FiM layer at the FiM/NM interface [40]. Because of the conservation of angular momentum, the loss of the angular momentum of the FiM layer leads to the enhancement of the damping coefficient by $\Delta\alpha = \frac{\gamma\hbar \mathrm{Re}(g_{\mathrm{eff}}^{\uparrow\downarrow})}{4\pi M_s t_{\mathrm{F}}}$, where $\hbar$, Re$(g_{\mathrm{eff}}^{\uparrow\downarrow})$, and t_{F} are the reduced Plank constant, the real part of the effective spin-mixing conductance, and the thickness of the FiM layer $(t_{\mathrm{F}} = 4$ nm), respectively. Here we exploited $\mathrm{Re}(g_{\mathrm{eff}}^{\uparrow\downarrow}) = 3.5 \times 10^{18}$ m^{-2} for the Pt/FiM bilayer [41].

In the coupled FiM system, since the damping increment includes the contributions of spin pumping from the left and right FiM layers [Fig. 5(a)] [42], the variation of the effective damping constant can be expressed as $\alpha'_{\mathrm{eff}} = \alpha_{\mathrm{eff}} + \alpha_{\mathrm{left}} + \alpha_{\mathrm{right}}$. Notably, the transfer of angular momentum between Pt and FiM was governed by FeCo via *s*-*d* exchange [41]. The spin-pumping-induced damping increase was thus expressed as $\alpha_{\mathrm{left}} = \alpha_{\mathrm{right}} = \frac{\Delta\alpha_{\mathrm{FeCo}} L_1}{|L_1 - L_2|}$, where $L_{i,i=1,2} = \frac{M_i}{\gamma_i}$, and $\Delta\alpha_{\mathrm{FeCo}} = \frac{\gamma\hbar \mathrm{Re}(g_{\mathrm{eff}}^{\uparrow\downarrow})}{4\pi M_{\mathrm{FeCo}} t_{\mathrm{F}}}$. Based on these principles, the partial PT symmetry was still well kept under the spin-pumping-induced variation of damping [Fig. 5(c)].

IV. CONCLUSIONS

In summary, our study presents the NH spin dynamics of a coupled FiM system, which is strictly relevant to the ratio of spins between the two sublattices in the FiM system. At the angular momentum compensation point, the spin dynamics described by the Néel vector satisfies the PT symmetry, exhibiting power-law frequency splitting concerning external perturbations at the EP with a fixed power of 1/2. However, when the ratio of spins between the two sublattices deviates from the angular momentum compensation point, the NH FiM system exhibits the coalescence of two out of three real eigenfrequencies at the EP and displays a variable power-law relationship between the frequency splitting and perturbations. This variability mirrors the feedback-induced frequency changes observed in coupled RLC circuits, where two frequency-relevant capacitances are involved.

ACKNOWLEDGMENTS

This work was supported by the National Key R&D Program of China (Grants No. 2022YFE0103300 and No. 2022YFB4401700) and the National Natural Science Foundation of China (NSFC) (Grant No. 12104301). The authors also acknowledge valuable suggestions offered by Prof. Peng Yan of the University of Electronic Science and Technology.

APPENDIX A: DERIVATION OF THE HAMILTONIAN H

We started with the LLG equations for the spin dynamics of the coupled FiM system:

$$\dot{\vec{S}}_1 = \vec{S}_1 \times (A_1\vec{S}_2 + B_1\vec{S}_3) + C_1\vec{S}_1 \times \dot{\vec{S}}_1 \,, \tag{A1}$$

$$\dot{\vec{S}}_3 = \vec{S}_3 \times (A_2\vec{S}_1 + B_2\vec{S}_4) + C_3\vec{S}_3 \times \dot{\vec{S}}_3 \,, \tag{A2}$$

$$\dot{\vec{S}}_2 = \vec{S}_2 \times (A_1\vec{S}_1 + B_1\vec{S}_4) + C_2\vec{S}_2 \times \dot{\vec{S}}_2 \,, \tag{A3}$$

$$\dot{\vec{S}}_4 = \vec{S}_4 \times (A_2\vec{S}_2 + B_2\vec{S}_3) + C_4\vec{S}_4 \times \dot{\vec{S}}_4 \,. \tag{A4}$$

Here $A_1 = -\gamma_\alpha J_R,\ A_2 = -\gamma_\beta J_A,\ B_1 = -\gamma_\alpha J_A,\ B_2 = -\gamma_\beta J_R,\ C_1 = \frac{\alpha}{S_{1s}}, C_2 = -\frac{\alpha}{S_{2s}}, C_3 = \frac{\alpha}{S_{3s}}$, and $C_4 = -\frac{\alpha}{S_{4s}}$, where $\gamma_{\alpha(\beta)}$ is the gyromagnetic ratio, and α is the damping constant. J_A and J_R represent the strength of AFM and RKKY interactions.

Under linear approximation, the spin can be approximated as $S_i(t) \cong S_{is}\vec{z} + (s_{ix}\vec{x} + s_{iy}\vec{y})e^{-\mathrm{i}wt},\ i = 1,2,3,4$. $S_{1s(2s)} = S_\alpha = (1 - x_G)S_{\mathrm{FeCo},s}$, and $S_{3s(4s)} = S_\beta = -x_G S_{\mathrm{Gd},s}$. x_G is defined as the atomic percentage of Gd in the FiM layer. We further defined $\psi_{n,i} = s_{ix} + is_{iy}$, and converted the LLG equations to

$$\dot{\Psi}_1 = iD_I\Psi_1 - iC_I\dot{\Psi}_1 - iA_I\Psi_2 - iB_I\Psi_3 \,, \tag{A5}$$

$$\dot{\Psi}_2 = iD_I\Psi_2 + iC_I\dot{\Psi}_2 - iA_I\Psi_1 - iB_I\Psi_4 \,, \tag{A6}$$

$$\dot{\Psi}_3 = iD_{II}\Psi_3 - iC_{II}\dot{\Psi}_3 - iA_{II}\Psi_1 - iB_{II}\Psi_4 \,, \tag{A7}$$

$$\dot{\Psi}_4 = iD_{II}\Psi_4 + iC_{II}\dot{\Psi}_4 - iA_{II}\Psi_2 - iB_{II}\Psi_3 \,. \tag{A8}$$

$A_{\mathrm{I}} = A_1S_\alpha, A_{\mathrm{II}} = A_2S_\beta,\ B_{\mathrm{I}} = B_1S_\alpha,\ B_{\mathrm{II}}=B_2S_\beta,\ C_{\mathrm{I}} = C_1,\ C_{\mathrm{II}} = C_3,\ D_{\mathrm{I}} = A_1S_\alpha - B_1S_\beta,\ D_{\mathrm{II}} = A_2S_\alpha - B_2S_\beta$. Finally, the LLG equations can been expressed as

$$(1 - iC_IS_\alpha)\dot{\Psi}_1 = -iD_I\Psi_1 + i(A_I\Psi_2 + B_I\Psi_3) \,, \tag{A9}$$

$$(1 + iC_IS_\alpha)\dot{\Psi}_2 = -iD_I\Psi_2 + i(A_I\Psi_1 + B_I\Psi_4) \,, \tag{A10}$$

$$(1 - iC_{II}S_\beta)\dot{\Psi}_3 = -iD_{II}\Psi_3 + i(A_{II}\Psi_1 + B_{II}\Psi_4) \,, \tag{A11}$$

$$(1 + iC_{II}S_\beta)\dot{\Psi}_4 = -iD_{II}\Psi_4 + i(A_{II}\Psi_2 + B_{II}\Psi_3) \,. \tag{A12}$$

Equations (A9)–(A12) can be expressed in the form of an eigenvalue equation as

$$\omega\begin{bmatrix}\psi_1\\ \psi_2\\ \psi_3\\ \psi_4\end{bmatrix} = \frac{1}{1+\alpha^2}\begin{bmatrix}-D_{\mathrm{I}}(1-i\alpha) & A_{\mathrm{I}}(1-i\alpha) & B_{\mathrm{I}}(1-i\alpha) & 0\\ A_{\mathrm{I}}(1+i\alpha) & -D_{\mathrm{I}}(1+i\alpha) & 0 & B_{\mathrm{I}}(1+i\alpha)\\ A_{\mathrm{II}}(1-i\alpha) & 0 & -D_{\mathrm{II}}(1-i\alpha) & B_{\mathrm{II}}(1-i\alpha)\\ 0 & A_{\mathrm{II}}(1+i\alpha) & B_{\mathrm{II}}(1+i\alpha) & -D_{\mathrm{II}}(1+i\alpha)\end{bmatrix}\begin{bmatrix}\psi_1\\ \psi_2\\ \psi_3\\ \psi_4\end{bmatrix}. \tag{A13}$$

APPENDIX B: DERIVATION OF THE SPIN DYNAMICS EQUATIONS FOR THE COUPLED FiM SYSTEMS WITH $\mathcal{PT}$ SYMMETRY

To derive the dynamics equations of the Néel vector, we first define $\vec{s} = \frac{\vec{s_\alpha}+\vec{s_\beta}}{2}$, $\vec{n} = \frac{\vec{s_\alpha}-\vec{s_\beta}}{2}$. Based on Eqs. (A1) and (A2) in the main text, we have

$$\begin{aligned}\frac{S_\alpha}{\gamma_\alpha}\dot{\vec{s}}_1 + \frac{S_\beta}{\gamma_\beta}\dot{\vec{s}}_3 = &-J_R(\vec{S}_1 \times \vec{S}_2 + \vec{S}_3 \times \vec{S}_4)\\ &+\alpha\left[\frac{S_\alpha}{\gamma_\alpha}(\vec{s}_1 \times \dot{\vec{s}}_1) + \frac{S_\beta}{\gamma_\beta}(\vec{s}_3 \times \dot{\vec{s}}_3)\right].\end{aligned} \tag{B1}$$

The left-hand side of Eq. (B1) can be written as $\rho\dot{\vec{s}}_{\mathrm{I}} + \delta_s\dot{\vec{n}}_{\mathrm{I}}$, where $\rho = \frac{S_\alpha}{\gamma_\alpha} + \frac{S_\beta}{\gamma_\beta}$, $\delta_s = \frac{S_\alpha}{\gamma_\alpha} - \frac{S_\beta}{\gamma_\beta}$. The first term on the right-hand side of Eq. (B1) can be expressed as $\vec{S}_1 \times \vec{S}_2 + \vec{S}_3 \times \vec{S}_4 = S_\alpha^2(\vec{s}_1 \times \vec{s}_2) + S_\beta^2(\vec{s}_3 \times \vec{s}_4)$, where $\vec{s}_1 = \vec{s}_{\mathrm{I}} + \vec{n}_{\mathrm{I}},\ \vec{s}_2 = \vec{s}_{\mathrm{II}} + \vec{n}_{\mathrm{II}}, \vec{s}_3 = \vec{s}_{\mathrm{I}} - \vec{n}_{\mathrm{I}}, \vec{s}_4 = \vec{s}_{\mathrm{II}} - \vec{n}_{\mathrm{II}}$. Therefore, $\vec{S}_1 \times \vec{S}_2 + \vec{S}_3 \times \vec{S}_4$ can be converted to

$$\begin{aligned}\vec{S}_1 \times \vec{S}_2 + \vec{S}_3 \times \vec{S}_4 = &\left(S_\alpha^2 + S_\beta^2\right)[(\vec{s}_{\mathrm{I}} \times \vec{s}_{\mathrm{II}}) + (\vec{n}_{\mathrm{I}} \times \vec{n}_{\mathrm{II}})]\\ &+ \left(S_\alpha^2 - S_\beta^2\right)[(\vec{s}_{\mathrm{I}} \times \vec{n}_{\mathrm{II}}) + (\vec{n}_{\mathrm{I}}\times\vec{s}_{\mathrm{II}})]\\ &\approx \left(S_\alpha^2 + S_\beta^2\right)(\vec{n}_{\mathrm{I}} \times \vec{n}_{\mathrm{II}}) \,.\end{aligned} \tag{B2}$$

It is easy to show that

$$\vec{s}_{\mathrm{I}} \times \dot{\vec{s}}_{\mathrm{I}} + \vec{n}_{\mathrm{I}} \times \dot{\vec{n}}_{\mathrm{I}} = \vec{s}_1 \times \dot{\vec{s}}_1 + \vec{s}_3 \times \dot{\vec{s}}_3,$$

$$\vec{s}_{\mathrm{I}} \times \dot{\vec{n}}_{\mathrm{I}} + \vec{n}_{\mathrm{I}} \times \dot{\vec{s}}_{\mathrm{I}} = \vec{s}_1 \times \dot{\vec{s}}_1 - \vec{s}_3 \times \dot{\vec{s}}_3.$$

As a result, under the linear approximation, the second term on the right-hand side of Eq. (B1) is

$$\alpha\left[\frac{S_\alpha}{\gamma_\alpha}(\vec{s}_1 \times \dot{\vec{s}}_1) + \frac{S_\beta}{\gamma_\beta}(\vec{s}_3 \times \dot{\vec{s}}_3)\right] \approx \alpha\rho(\vec{n}_{\mathrm{I}} \times \dot{\vec{n}}_{\mathrm{I}}). \tag{B3}$$

Based on Eqs. (B2) and (B3), we can derive

$$\rho\dot{\vec{s}}_{\mathrm{I}} + \delta_s\dot{\vec{n}}_{\mathrm{I}} = -J_R\left(S_\alpha^2 + S_\beta^2\right)(\vec{n}_{\mathrm{I}} \times \vec{n}_{\mathrm{II}}) + \alpha\rho(\vec{n}_{\mathrm{I}} \times \dot{\vec{n}}_{\mathrm{I}}) \,. \tag{B4}$$

Via similar derivation, we also have

$$\begin{aligned}\rho\dot{\vec{n}}_{\mathrm{I}} + \delta_s\dot{\vec{s}}_{\mathrm{I}} = &J_R(\vec{S}_3 \times \vec{S}_4 - \vec{S}_1 \times \vec{S}_2)\\ &+ J_A(\vec{S}_3 \times \vec{S}_1 - \vec{S}_1 \times \vec{S}_3)\\ &+ \alpha\rho[(\vec{n}_{\mathrm{I}} \times \dot{\vec{s}}_{\mathrm{I}}) + (\vec{s}_{\mathrm{I}} \times \dot{\vec{n}}_{\mathrm{I}})]\\ &+ \alpha\delta_s[(\vec{s}_{\mathrm{I}} \times \dot{\vec{s}}_{\mathrm{I}}) + (\vec{n}_{\mathrm{I}} \times \dot{\vec{n}}_{\mathrm{I}})] \,.\end{aligned} \tag{B5}$$

By keeping the leading term, Eq. (B5) can be approximately written as

$$\rho\dot{\vec{n}}_{\mathrm{I}} \approx 4J_A S_\alpha S_\beta(\vec{s}_{\mathrm{I}} \times \vec{n}_{\mathrm{I}})\ . \tag{B6}$$

By defining $A_{\mathrm{ex}} = 4J_A S_\alpha S_\beta$ and crossing product $\vec{n}_{\mathrm{I}}$ at the two sides of Eq. (B4), we further deduced

$$\vec{s}_{\mathrm{I}} \approx -\frac{\rho}{A_{\mathrm{ex}}}\dot{\vec{n}}_{\mathrm{I}} \times \vec{n}_{\mathrm{I}}\ . \tag{B7}$$

Combining Eq. (B7) and Eq. (B4), we have

$$\begin{aligned} &-\frac{\rho^2}{A_{\mathrm{ex}}}(\ddot{\vec{n}}_{\mathrm{I}} \times \vec{n}_{\mathrm{I}}) + \delta_s\dot{\vec{n}}_1 \\ &\quad = -J_R\left(S_\alpha^2 + S_\beta^2\right)(\vec{n}_{\mathrm{I}} \times \vec{n}_{\mathrm{II}}) + \alpha\rho(\vec{n}_{\mathrm{I}} \times \dot{\vec{n}}_{\mathrm{I}}) \end{aligned} \tag{B8}$$

$$-\frac{\rho^2}{A_{\mathrm{ex}}}\ddot{\vec{n}}_{\mathrm{I}} + \delta_s(\dot{\vec{n}}_{\mathrm{I}} \times \vec{n}_{\mathrm{I}}) \doteq -J_R\left(S_\alpha^2 + S_\beta^2\right)(\vec{n}_{\mathrm{II}} - \vec{n}_{\mathrm{I}}) + \alpha\rho\dot{\vec{n}}_{\mathrm{I}} \tag{A9}$$

For FiM system II, based on the same derivation, we deduced

$$-\frac{\rho^2}{A_{\mathrm{ex}}}\ddot{\vec{n}}_{\mathrm{II}} + \delta_s(\vec{n_{\mathrm{II}}}\ \times \vec{n}_{\mathrm{II}}) \doteq -J_R\left(S_\alpha^2 + S_\beta^2\right)(\vec{n}_{\mathrm{I}} - \vec{n}_{\mathrm{II}}) + \alpha\rho\dot{\vec{n}}_{\mathrm{II}} \tag{B10}$$

APPENDIX C: EIGENVALUE OF HAMILTONIAN *H*

Based on this equation, we deduce the eigenfrequencies as below:

$$f_{1,2} = \left[-\tfrac{1}{2}A(1+i) \mp \sqrt{3}B - \tfrac{1}{2}B + C\right]/2\pi\ , \tag{C1}$$

$$f_3 = (A + B + C)/2\pi\ . \qquad \text{C2)}$$

Here the negative (positive) sign is for f_1 (f_2). A, B, and C can be expressed by the different frequency components $\omega_{R\alpha} = \gamma_\alpha J_R S_\alpha$, $\omega_{R\beta} = \gamma_\beta J_R S_\beta$, $\omega_{A\alpha} = \gamma_\alpha J_A S_\beta$, $\omega_{A\beta} = \gamma_\beta J_A S_\alpha$. $A = \sqrt[3]{(\sqrt{-F^3 + (CI + I')^2} + CI + I')}$, $B = \frac{F}{A}$, $C = \frac{2}{3}((\omega_{R\alpha} - \omega_{R\beta}) + (\omega_{A\beta} - \omega_{A\alpha}))$, $F = C^2 + \frac{1}{3}D$, $I = \frac{1}{2}D$. Here $D = -(\omega_{A\beta} - \omega_{A\alpha})^2(1 + \alpha^2) - 4\omega_{R\alpha}\omega_{R\beta} - 4(\omega_{R\alpha}\omega_{A\beta} + \omega_{R\beta}\omega_{A\alpha}) + 2(1 + \alpha^2)(\omega_{R\alpha}\omega_{A\alpha} + \omega_{R\beta}\omega_{A\beta})$, $I' = C^3 + 2[\omega_{A\beta}\omega_{A\alpha}(\omega_{R\beta} - \omega_{R\alpha}) + \omega_{R\alpha}\omega_{R\beta}(\omega_{A\alpha} - \omega_{A\beta})]$.

---

[1] S. K. Kim, G. S. Beach, K.-J. Lee, T. Ono, T. Rasing, and H. Yang, Ferrimagnetic spintronics, Nat. Mater. **21**, 24 (2022).

[2] C. D. Stanciu, A. V. Kimel, F. Hansteen, A. Tsukamoto, A. Itoh, A. Kirilyuk, and T. Rasing, Ultrafast spin dynamics across compensation points in ferrimagnetic GdFeCo: The role of angular momentum compensation, Phys. Rev. B **73**, 220402(R) (2006).

[3] V. Yurlov, K. Zvezdin, P. Skirdkov, and A. Zvezdin, Domain wall dynamics of ferrimagnets influenced by spin current near the angular momentum compensation temperature, Phys. Rev. B **103**, 134442 (2021).

[4] C. O. Avci, E. Rosenberg, L. Caretta, F. Büttner, M. Mann, C. Marcus, D. Bono, C. A. Ross, and G. S. Beach, Interface-driven chiral magnetism and current-driven domain walls in insulating magnetic garnets, Nat. Nanotechnol. **14**, 561 (2019).

[5] J. Shim and K.-J. Lee, Enhanced magnon-magnon entanglement in the vicinity of an angular momentum compensation point of a ferrimagnet in a cavity, Phys. Rev. B **106**, L140408 (2022).

[6] C. M. Bender, Making sense of non-Hermitian Hamiltonians, Rep. Prog. Phys. **70**, 947 (2007).

[7] H. M. Hurst and B. Flebus, Non-Hermitian physics in magnetic systems, J. Appl. Phys. **132**, 220902 (2022).

[8] R. El-Ganainy, K. G. Makris, M. Khajavikhan, Z. H. Musslimani, S. Rotter, and D. N. Christodoulides, Non-Hermitian physics and PT symmetry, Nat. Phys. **14**, 11 (2018).

[9] C. M. Bender, S. Boettcher, and P. N. Meisinger, $\mathcal{PT}$-symmetric quantum mechanics, J. Math. Phys. **40**, 2201 (1999).

[10] W. Heiss, The physics of exceptional points, J. Phys. A Math. Theor. **45**, 444016 (2012).

[11] C. M. Bender and S. Boettcher, Real spectra in non-Hermitian Hamiltonians having *PT* symmetry, Phys. Rev. Lett. **80**, 5243 (1998).

[12] K. Deng, X. Li, and B. Flebus, Exceptional points as signatures of dynamical magnetic phase transitions, Phys. Rev. B **107**, L100402 (2023).

[13] M.-A. Miri and A. Alu, Exceptional points in optics and photonics, Science **363**, eaar7709 (2019).

[14] V. Achilleos, G. Theocharis, O. Richoux, and V. Pagneux, Non-Hermitian acoustic metamaterials: Role of exceptional points in sound absorption, Phys. Rev. B **95**, 144303 (2017).

[15] C. Shi, M. Dubois, Y. Chen, L. Cheng, H. Ramezani, Y. Wang, and X. Zhang, Accessing the exceptional points of parity-time symmetric acoustics, Nat. Commun. **7**, 11110 (2016).

[16] H. Liu, D. Sun, C. Zhang, M. Groesbeck, R. Mclaughlin, and Z. V. Vardeny, Observation of exceptional points in magnonic parity-time symmetry devices, Sci. Adv. **5**, eaax9144 (2019).

[17] Y. Tserkovnyak, Exceptional points in dissipatively coupled spin dynamics, Phys. Rev. Res. **2**, 013031 (2020).

[18] C. M. Bender, PT symmetry, in *Time and Science: Volume 3: Physical Sciences and Cosmology* (World Scientific, Singapore, 2023), p. 285.

[19] H. Hodaei, A. U. Hassan, S. Wittek, H. Garcia-Gracia, R. El-Ganainy, D. N. Christodoulides, and M. Khajavikhan, Enhanced sensitivity at higher-order exceptional points, Nature (London) **548**, 187 (2017).

[20] W. Chen, Ş. Kaya Özdemir, G. Zhao, J. Wiersig, and L. Yang, Exceptional points enhance sensing in an optical microcavity, Nature (London) **548**, 192 (2017).

[21] C. Zeng, Y. Sun, G. Li, Y. Li, H. Jiang, Y. Yang, and H. Chen, Enhanced sensitivity at high-order exceptional points in a passive wireless sensing system, Opt. Express **27**, 27562 (2019).

[22] T. Yu, H. Yang, L. Song, P. Yan, and Y. Cao, Higher-order exceptional points in ferromagnetic trilayers, Phys. Rev. B **101**, 144414 (2020).

[23] K. Yin, X. Hao, Y. Huang, J. Zou, X. Ma, and T. Dong, High-order exceptional points in pseudo-Hermitian radio-frequency circuits, Phys. Rev. Appl. **20**, L021003 (2023).

[24] H. Yang, C. Wang, T. Yu, Y. Cao, and P. Yan, Antiferromagnetism emerging in a ferromagnet with gain, Phys. Rev. Lett. **121**, 197201 (2018).

[25] J. Lee, T. Kottos, and B. Shapiro, Macroscopic magnetic structures with balanced gain and loss, Phys. Rev. B **91**, 094416 (2015).

[26] A. Galda and V. M. Vinokur, Parity-time symmetry breaking in magnetic systems, Phys. Rev. B **94**, 020408(R) (2016).

[27] M. Bersweiler, D. Lacour, K. Dumesnil, F. Montaigne, and M. Hehn, Phase diagram in exchange-coupled CoTb/[Co/Pt] multilayer-based magnetic tunnel junctions, Phys. Rev. B **92**, 224431 (2015).

[28] S. Mi, S. H. Yuan, and P. Lyu, Size effect of Ruderman-Kittel-Kasuya-Yosida interaction mediated by electrons in nanoribbons, J. Appl. Phys. **109**, 083931 (2011).

[29] I. Radu, K. Vahaplar, C. Stamm, T. Kachel, N. Pontius, H. Dürr, T. Ostler, J. Barker, R. Evans, and R. Chantrell, Transient ferromagnetic-like state mediating ultrafast reversal of antiferromagnetically coupled spins, Nature (London) **472**, 205 (2011).

[30] K. Cai, Z. Zhu, J. M. Lee, R. Mishra, L. Ren, S. D. Pollard, P. He, G. Liang, K. L. Teo, and H. Yang, Ultrafast and energy-efficient spin-orbit torque switching in compensated ferrimagnets, Nat. Electron. **3**, 37 (2020).

[31] See Supplemental Material at http://link.aps.org/supplemental/10.1103/PhysRevB.109.184426 for the influence of these additional factors on the NH dynamics of the coupled FiM system.

[32] A. Kamra, R. E. Troncoso, W. Belzig, and A. Brataas, Gilbert damping phenomenology for two-sublattice magnets, Phys. Rev. B **98**, 184402 (2018).

[33] V. Pachkawade, A new readout method for a high sensitivity capacitance sensor based on weakly coupled resonators, Eng. Proc. **2**, 86 (2020).

[34] X.-L. Xu, H.-Q. Li, and J.-S. Wang, The quantum fluctuations of mesoscopic damped mutual capacitance coupled double resonance RLC circuit in excitation state of the squeezed vacuum state, Int. J. Theor. Phys. **45**, 2471 (2006).

[35] J. Schindler, A. Li, M. C. Zheng, F. M. Ellis, and T. Kottos, Experimental study of active LRC circuits with PT symmetries, Phys. Rev. A **84**, 040101(R) (2011).

[36] T. Helbig, T. Hofmann, S. Imhof, M. Abdelghany, T. Kiessling, L. Molenkamp, C. Lee, A. Szameit, M. Greiter, and R. Thomale, Generalized bulk–boundary correspondence in non-Hermitian topolectrical circuits, Nat. Phys. **16**, 747 (2020).

[37] F. Tsui, C. Flynn, M. Salamon, J. Borchers, R. Erwin, and J. Rhyne, Layer thickness dependence of anisotropic coupling in Gd/Y superlattices, J. Magn. Magn. Mater. **104**, 1901 (1992).

[38] C. Davut, C. Deger, and F. Yildiz, Enhanced magneto-optical activity of multilayer thin films: A novel platform for magnetic nanoparticle sensing, Meas. Sci. Technol. **31**, 015104 (2019).

[39] E. R. García Barroso, P. D. González Pérez, and P. Popescu-Pampu, Variations on inversion theorems for Newton–Puiseux series, Math. Ann. **368**, 1359 (2017).

[40] Y. Tserkovnyak, A. Brataas, and G. E. Bauer, Enhanced Gilbert damping in thin ferromagnetic films, Phys. Rev. Lett. **88**, 117601 (2002).

[41] Y. Li, D. Zheng, B. Fang, C. Liu, C. Zhang, A. Chen, Y. Ma, K. Shen, H. Liu, and A. Manchon, Unconventional spin pumping and magnetic damping in an insulating compensated ferrimagnet, Adv. Mater. **34**, 2200019 (2022).

[42] B. Heinrich, Y. Tserkovnyak, G. Woltersdorf, A. Brataas, R. Urban, and G. E. Bauer, Dynamic exchange coupling in magnetic bilayers, Phys. Rev. Lett. **90**, 187601 (2003).